Nonlinear enhancement of the fractal structure in the escape dynamics of Bose-Einstein condensates

Kevin A. Mitchell and Boaz Ilan
School of Natural Sciences, University of California, Merced, California 95344, USA
(Received 1 July 2009; published 8 October 2009)

We consider the escape dynamics of an ensemble of Bose-Einstein-condensed atoms from an optical-dipole trap consisting of two overlapping Gaussian wells. Earlier theoretical studies (based on a model of quantum evolution using ensembles of classical trajectories) predicted that self-similar fractal features could be visible in this system by measuring the escaping flux as a function of time for varying initial conditions. Here, direct numerical quantum simulations show the clear influence of quantum interference on the escape data. Fractal features are still evident in the data, albeit with interference fringes superposed. Furthermore, the nonlinear influence of atom-atom interactions is also considered, in the context of the (2+1)-dimensional Gross-Pitaevskii equation. Of particular note is that an attractive nonlinear interaction enhances the resolution of fractal structures in the escape data. Thus, the interplay between nonlinear focusing and dispersion results in dynamics that resolve the underlying classical fractal more faithfully than the noninteracting quantum (or classical) dynamics.

DOI: 10.1103/PhysRevA.80.043406 PACS number(s): 37.10.Gh, 05.45.Ac, 05.45.Df, 05.45.Mt

I. INTRODUCTION

The Hamiltonian evolution of a classical or quantum ensemble through (phase) space under chaotic dynamics governs numerous and diverse physical phenomena, including the ionization of atoms in external fields [1–19], the emission of light from lasing microbeads [20,21], chaotic advection in fluids at low Reynolds number [22–26], and the transport of comets, asteroids, and spacecraft in the solar system [27,28]. Furthermore, it has long been appreciated that such chaotic transport processes generate self-similar fractal structures. Though this fractal geometry is manifest in the dynamics of individual classical trajectories, in practice, the visualization of individual trajectories and their associated fractal structure is limited by the inherent instabilities of the chaotic system. That is, an initially localized ensemble designed to follow a given chaotic trajectory will rapidly disperse throughout the available phase space.

Atomic systems, due to their insensitivity to external perturbations and high degree of control, have proved to be very effective for the experimental and theoretical study of chaos, both classical and quantum [29]. Initial studies of chaos in atomic physics focused on the electron dynamics within an atom, typically with an applied electric or magnetic field [1–19]. More recently, however, consideration has been given to chaotic dynamics in the position degree of freedom for the trapped atoms themselves [30–41]. For example, Raizen and co-workers [40] and Davidson and co-workers [41] independently demonstrated that the long-time decay rate of ultracold atoms from an open optical billiard trap would show a characteristic exponential decay for fully developed chaos and an algebraic decay for regular (nonchaotic) dynamics. Subsequently, Ref. [42] predicted that the *early time* escape dynamics of ultracold or Bose-Einstein-condensed atoms from an optical trap could be used to directly image fractal structures over several orders of self-similarity. The analysis in Ref. [42] was motivated by related studies of the time-dependent chaotic ionization of hydrogen in applied electric and magnetic fields [16–18]; after an excitation by an initial laser pulse, the hydrogen atom is predicted to emit a chaos-induced train of electron pulses, which reflects the underlying fractal structure of the dynamics. However, compared to ionization dynamics, atomic traps have certain advantages, such as flexibility in tailoring the optical potential, direct control over the shape and placement of the initial ensemble, and direct access to measuring the subsequent distribution of the ensemble as a function of time.

Reference [42] modeled the time evolution of the Bose-Einstein condensate (BEC) within a chaotic trapping potential using a *classical* ensemble of noninteracting atoms. Here, we study this dynamics using a full quantum simulation based on both the linear (2+1)-dimensional Schrödinger equation as well as the (nonlinear) Gross-Pitaevskii equation. The impact of interference as well as atom-atom interactions on the resolution of the fractal structure in the escape dynamics is investigated. The Schrödinger analysis yields a fractal structure that follows the classical density, except with interference fringes superposed. When atom-atom interactions are taken into account via the Gross-Pitaevskii equation, we find that a modest repulsive interaction does not destroy the fractal features, though for large enough interactions, the fractal structure is washed out. More interestingly, a strong attractive interaction between the atoms induces a considerable enhancement of the fractal structure. This can be understood as the attractive interactions partially offsetting the inherent dispersion of the state, so that the state more faithfully tracks the central trajectory of the classical dynamics. Such reduction in dispersion has been dramatically demonstrated in the experimental observation of BEC solitons in one dimension [43–45]. A critical distinction here is our use of a *two*-dimensional and *chaotic* potential.

In this work, it is important to distinguish between two separate "nonlinear" effects. There is the classical nonlinearity of the chaotic potential, which causes neighboring trajectories to diverge exponentially from one another. There is also the cubic wave-function nonlinearity $|\Psi|^2\Psi$ in the

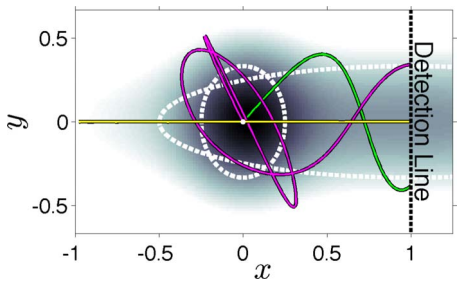

FIG. 1. (Color online) The trapping potential (1) is shown by the shading. The size of each Gaussian is denoted by an ellipse. Three trajectories launched from the origin are shown, with launch angles θ=0.85, 2.04, and π.

Gross-Pitaevskii equation. As mentioned above, for the focusing case these two effects are in competition and partially balance.

This paper is organized as follows. In Sec. II we describe the basic geometry of the optical trap, the initial conditions of the atomic state, and the detection scheme. In Sec. III we review the classical trap dynamics described in Ref. [42]. Section IV presents our classical and quantum models of BEC evolution, along with the numerical results. Notably, Sec. IV C discusses how the time-dependent escaping atomic flux depends on the initial launch angle of the condensate. We focus on the resolution of fractal features in the data. Section V demonstrates how the fractal resolution can be enhanced by decreasing the effective Planck's constant.

II. SETUP OF THE ATOMIC TRAP

Following Ref. [42], we consider a two-dimensional optical-dipole trap constructed from two overlapping Gaussian beams, giving rise to an asymmetric double-well potential

$$V(x,y) = -V_1 \exp\left(-\frac{x^2}{2\sigma_{1x}^2} - \frac{y^2}{2\sigma_{1y}^2}\right) - V_2 \exp\left(-\frac{(x-x_2)^2}{2\sigma_{2x}^2} - \frac{y^2}{2\sigma_{2y}^2}\right), \quad (1)$$

where x_2 measures the distance between the wells, V_1 and V_2 measure the depths of the wells, and where σ_{1x}, σ_{1y}, σ_{2x}, and σ_{2y} measure the x and y widths of the wells (Fig. 1) Furthermore, the atoms are assumed to be constrained in the z direction, so that the z dynamics can be ignored. (More precisely, we assume a uniform density in the z direction.)

The variables in Eq. (1) are dimensionless scaled variables defined relative to the physical length scale X_0 and energy scale E_0. The unscaled "physical" variables denoted by tildes are thus

$$\tilde{x} = xX_0, \quad \tilde{y} = yX_0,$$

$$\tilde{x}_2 = x_2X_0, \quad \tilde{V}_i = V_iE_0, \quad i = 1,2,$$

$$\tilde{\sigma}_{ij} = \sigma_{ij}X_0, \quad i = 1,2, \quad j = x,y. \quad (2)$$

We fix the dimensionless parameters of the potential to be those used in Ref. [42]

$$\sigma_{1x} = 0.25, \quad \sigma_{1y} = 0.333, \quad x_2 = 1,$$

$$\sigma_{2x} = 1.5, \quad \sigma_{2y} = 0.333, \quad V_1 = V_2 = 1. \quad (3)$$

Note that these choices imply that the length scale X_0 equals the separation distance $\tilde{x}_2$ between the Gaussians and that the energy scale E_0 equals the depths $\tilde{V}_i$, i=1,2, of the Gaussians. As seen in Fig. 1, the right Gaussian is highly elongated in the y direction, whereas the left Gaussian is fairly isotropic. Though the depth of each Gaussian individually is the same, the manner of their overlap is such that the left well is much deeper than the right. Importantly, this potential is nonseparable and exhibits strong classical chaos.

By changing the power, shape, and position of the laser beams, the length and energy scales X_0 and E_0 (i.e., the size and depth of the potential) can be experimentally adjusted, while keeping the dimensionless parameters (3) fixed. Under such adjustments of scale, the classical dynamics remains invariant when expressed in dimensionless variables. However, the quantum dynamics is not invariant, as can be seen from the dimensionless scaled Planck's constant

$$\hbar = \tilde{\hbar}/(X_0P_0) = \tilde{\hbar}/(E_0T_0) = \tilde{\hbar}/(X_0\sqrt{M_0E_0}). \quad (4)$$

Here, $\tilde{\hbar}$ is the original dimension-full value of Planck's constant and M_0, T_0=$X_0(M_0/E_0)^{1/2}$, and P_0=$\sqrt{M_0E_0}$ are the mass, time, and momentum scales. The mass scale M_0 is chosen to be the atomic mass. Equation (4) shows how we can adjust the effective Planck's constant, while keeping the scaled classical mechanics invariant. For example, if the dimensionless parameters (3) and X_0 are held fixed and the laser power is increased by a factor of four, increasing the depth E_0 of the dipole potential by a factor of four, then the effective Planck's constant is reduced by a factor of two. The same effect could be achieved by scaling the size of the trap by a factor of two, while keeping the laser intensity at the center of each Gaussian beam fixed.

A detection line is created by a resonant laser sheet placed in the right well at x=x_2 and oriented in the y direction (Fig. 1). When atoms strike the detection line, they fluoresce and are subsequently kicked out of the trap. Since the detection line is placed just to the right of the saddle between the wells, any atoms that pass from the left well over the saddle into the right well will be detected and, furthermore, will never pass back into the left well. The right well thus acts as an exit channel for the trap.

Following Ref. [42], we utilize the following proposed protocol. At t=0, the atomic ensemble is loaded in the center (x=y=0) of the left Gaussian and given a "kick" in the launch direction θ, measured relative to the positive x axis. We assume that the kick simply results in an overall shift Δp in the momentum of the state. The mean energy of the resulting state is chosen to be E=−0.420. This value is above the potential saddle, so that transport into the right well can occur classically, without relying on quantum tunneling. As

atoms cross the saddle, they quickly reach the detection line, where their arrival is recorded as a function of time. Thus, this setup measures the outgoing flux of atoms striking the detection line as a function of time, for a given initial launch angle θ.

III. CLASSICAL DYNAMICS OF THE CENTRAL TRAJECTORY

The simplest model of the escape dynamics would be to approximate the evolution of the atomic state as a packet that simply follows the central trajectory. By the *central trajectory*, we mean the classical trajectory whose initial position and momentum are the expectation values $\langle \mathbf{r} \rangle$ and $\langle \mathbf{p} \rangle$ over the initial state. In this model, the outgoing flux measured at the detection line would be a short pulse centered at the time that the central trajectory crosses the line. As it does so, this pulse would also have undergone some (linear) dispersion relative to the initial state. For a harmonic potential, this model is valid for all time; but for a nonlinear, and in particular, a chaotic potential, this model may be valid for short times but it eventually breaks down. This breakdown is essentially a classical phenomenon. A classical ensemble following the central trajectory will first disperse linearly about the central trajectory. Eventually, however, it will disperse sufficiently so as to be influenced by the nonlinear terms about the central trajectory, resulting in the ensemble ultimately dispersing throughout the available (phase) space. Nevertheless, the central trajectory model gives an idealization appropriate in the limit that the position and momentum widths of the initial packet go to zero. We thus first consider the behavior of a single trajectory launched from the origin, with energy $E=-0.420$, as a function of the launch angle θ, measured relative to the positive x axis.

Figure 1 shows three classical trajectories beginning at the origin with $\theta=0.85$, 2.04, and π (in radians). The complexity and diversity of these paths illustrate the chaotic nature of the potential. The time for such a trajectory to escape, i.e., to reach the detector, is highly sensitive to its launch angle θ, as shown in the escape-time plot Fig. 2. This plot displays a fractal structure characteristic of chaotic escape and scattering functions [46–60]. It has an infinite number of smooth icicle-shaped regions [47], the edges of which go to infinite escape time. These regions, which we call simply icicles, occur at all scales in θ and at arbitrarily long times. They display a well defined self-similar structure, as illustrated by the expanded plots in Fig. 2. The expansions show one pattern, or template, of icicles that is repeated on smaller scales. In fact, the fractal structure is more complicated than even this suggests, as there are multiple such templates repeated recursively within one another on all scales within the *same* escape-time plot. Reference [42] discusses this in more detail and gives a symbolic encoding for the self-similar structure of Fig. 2. The study of such fractal structure and how it can be described using symbolic techniques has been extensively studied and is still an active area of research [51,52,54–68].

As noted above, the model of the packet following the central trajectory, with some (linear) dispersion, is valid when the position and momentum distribution of the initial state is sufficiently small and the escape time is sufficiently short. In this spirit, Ref. [42] argued that a small ensemble of ultracold atoms should have sufficient resolution to resolve several orders of the fractal structure in Fig. 2. The resolution was particularly pronounced below the BEC transition, where the state occupies essentially a single Planck cell. In the next section, after first reviewing the classical-ensemble model of Ref. [42], we compute the influence of quantum interference and atom-atom interactions on the fractal resolution.

IV. CHAOTIC ESCAPE DYNAMICS OF AN ATOMIC ENSEMBLE

A. Escape dynamics of a classical ensemble

We can improve upon the central trajectory approximation by numerically evolving an initial classical Gaussian ensemble, with phase-space probability distribution

$$\rho(\mathbf{r},\mathbf{p}) = \frac{1}{(\sigma_r \sigma_p 2\pi)^2} \exp\left(-\frac{r^2}{2\sigma_r^2} - \frac{|\mathbf{p}-\mathbf{p}_{c0}|^2}{2\sigma_p^2} \right), \tag{5}$$

where σ_r and σ_p are the position and momentum standard deviations, and where $\mathbf{p}_{c0}=p_{c0}(\cos\theta,\sin\theta)$ is the central momentum. Note that the magnitude p_{c0} of the central momentum is already determined by the mean ensemble energy $E=-0.420$, i.e., $p_{c0}=\sqrt{2[E-V(0,0)]}$. For a thermal (noncondensed) atomic state, the phase-space area $\sigma_r\sigma_p$ is considerably larger than $\hbar/2$. Restricting here to pure condensates, however, the atomic state occupies a single Planck cell in phase space and, hence, $\sigma_r\sigma_p=\hbar/2$. We divide the total uncertainty between position and momentum as

$$\sigma_r = s\sqrt{\frac{\hbar}{2}}, \quad \sigma_p = \frac{1}{s}\sqrt{\frac{\hbar}{2}}, \tag{6}$$

where $s=0.321$, so that σ_r and σ_p are of the same order of magnitude. Recalling that we can adjust $\hbar$ independently from the classical quantities, we set $\hbar=0.020\,4$, which places us solidly in the semiclassical regime.

The classical evolution of 5×10^4 initial points drawn from the distribution (5) is shown in the first column of Fig. 3, for launch angle $\theta=0.85$. In the first frame, the ensemble is closely following the central trajectory shown as the curve that begins at the origin and terminates at the large dot. In the second frame, the central trajectory is about to cross the detection line. The bulk of the ensemble, however, has already escaped at this time. This is seen in the escape-rate plot at the bottom of the first column, where the vertical line denotes the escape time of the central trajectory. Thus, the flux primarily exits as a single pulse occurring somewhat before the central trajectory. However, the second frame does show that a noticeable fraction of the ensemble has also reflected off the saddle. In the next two frames, this remaining ensemble spreads throughout the left well and slowly leaks across the saddle. Nevertheless, the main observation for this launch angle is that the classical dispersion is slow enough that most of the packet exits the trap as a single pulse that closely follows the central trajectory. We shall consider other launch

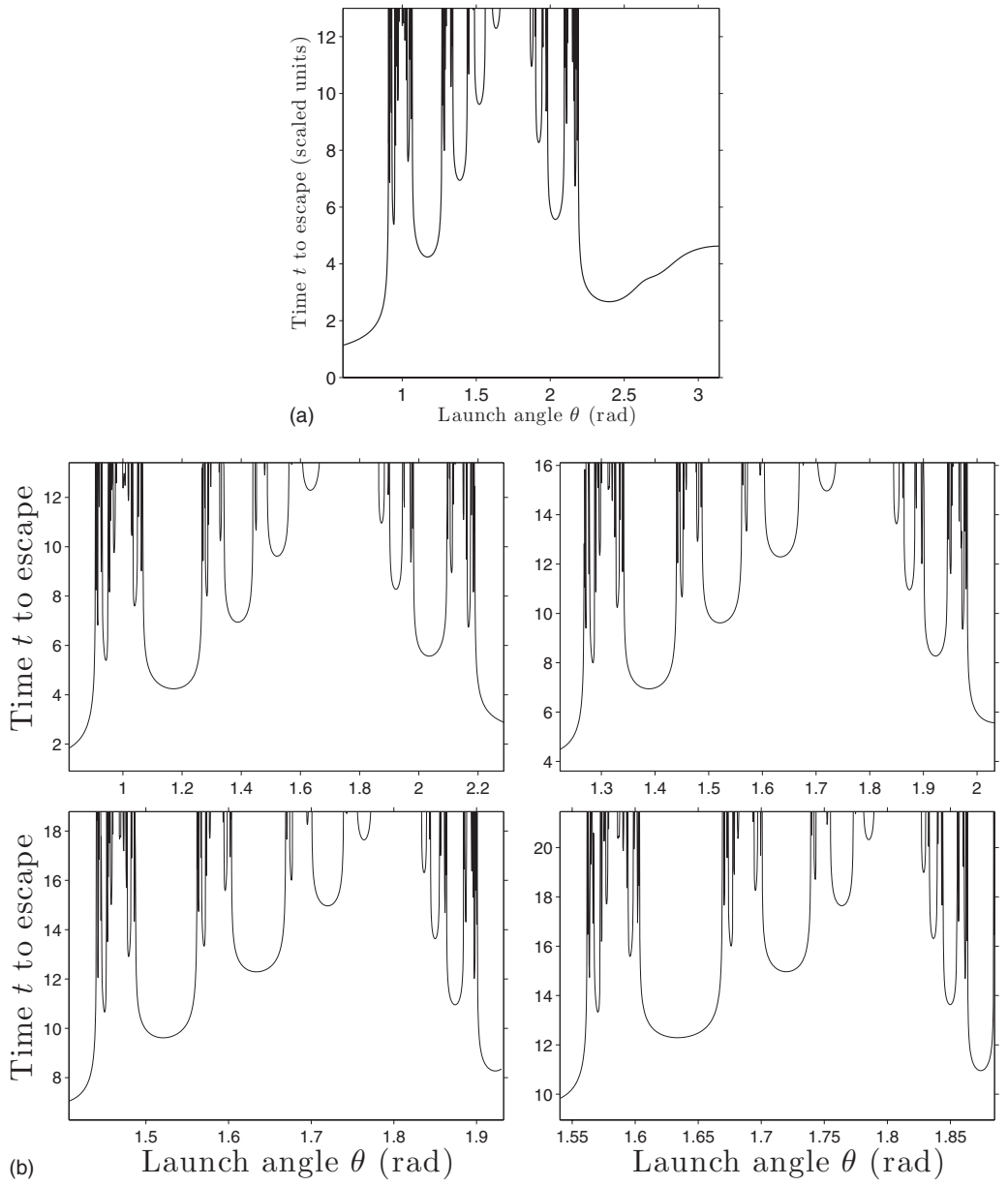

FIG. 2. The escape time for a trajectory launched from the origin with angle θ and with energy $E=-0.420$. The lower four frames are progressively larger expansions of the central region of the escape-time plot, illustrating the structural self-similarity of the function.

angles in Sec. IV C, but first we consider the quantum evolution.

B. Quantum analysis of the BEC dynamics

The classical model of the packet is appropriate for a thermal (i.e., noncondensed) atomic ensemble. It is also an appropriate model for a quantum packet, so long as the evolution time is short enough that the packet does not break up and interfere with itself.

At longer times, the correspondence between the classical and quantum evolution of wave packets has been well studied from the semiclassical perspective [69–71]. The basic picture is that the classical trajectories carry the quantum amplitude forward with a phase given by the classical action integrated along the trajectory. Thus, the quantum evolution follows the classical density, with interference fringes superposed due to overlapping trajectories. At a long enough time (on the order of $\log \hbar$), the classical ensemble develops small scale structure that the quantum amplitude is no longer able to resolve.

Though we are guided by the semiclassical perspective, our analysis here is based on a direct numerical computation of the BEC wave-packet evolution using the Gross-Pitaevskii equation [72,73]

$$i\hbar\frac{\partial}{\partial t}\Psi = -\frac{\hbar^2}{2}\left(\frac{\partial^2}{\partial x^2}+\frac{\partial^2}{\partial y^2}\right)\Psi + V\Psi + g|\Psi|^2\Psi, \qquad (7)$$

where we normalize the order parameter $\Psi(x,y,t)$ to unity, i.e., $\int|\Psi|^2dxdy=1$, and where we continue to work in the scaled variables of Sec. II. The cubic nonlinearity is the

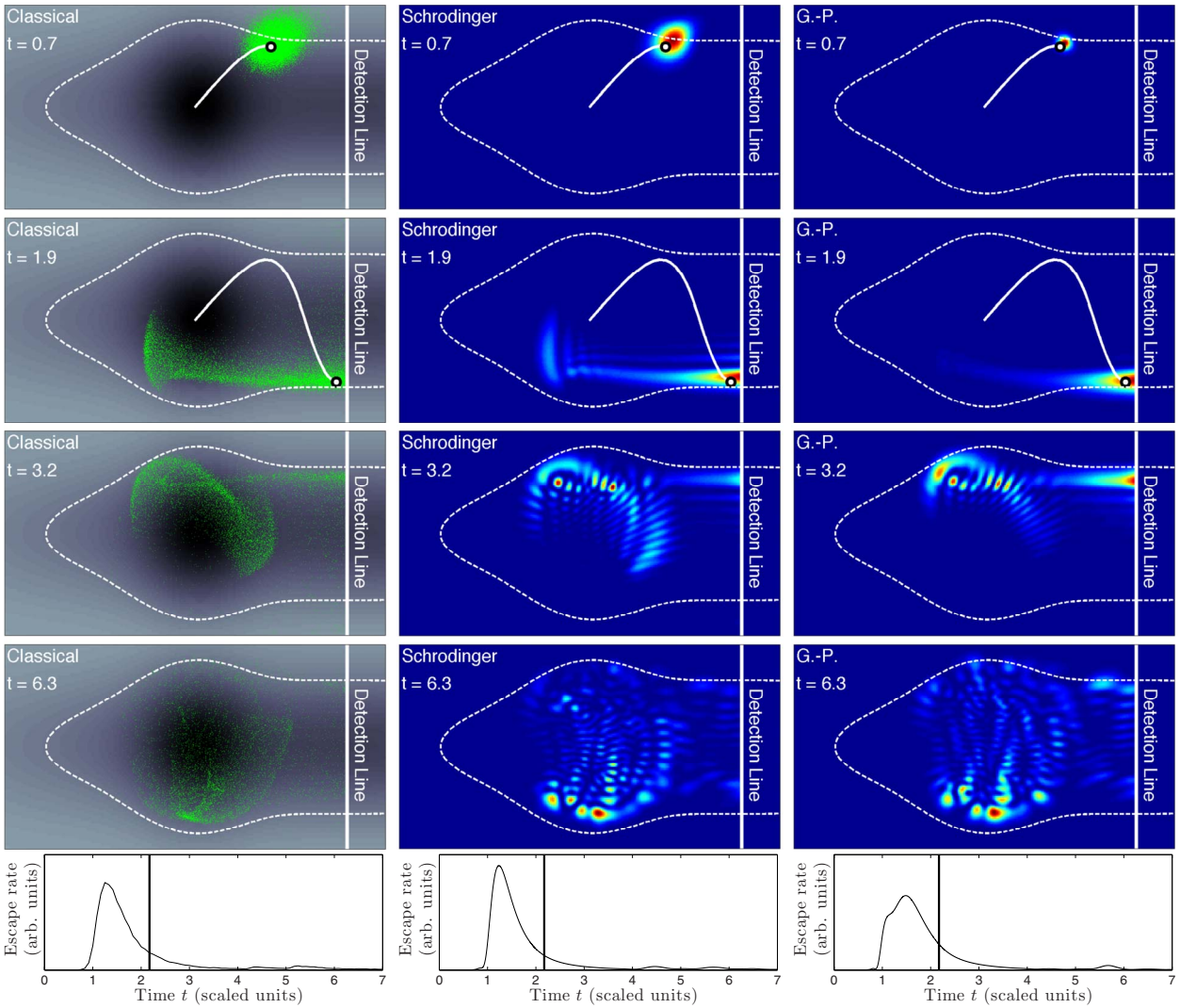

FIG. 3. (Color online) The evolution of the initial state as a function of time for launch angle $\theta=0.85$. Column 1 is a classical trajectory simulation using 5×10^4 trajectories. The curve beginning at the origin and terminating at the large dot illustrates the central trajectory up to the given value of t. (The central trajectory is not shown once it strikes the detection line.) The dashed curve forms the boundary of the classically allowed region for trajectories whose energy equals the mean energy $E=-0.420$ of the state. Column 2 is the Schrödinger simulation using an equivalent initial state. Column 3 is the Gross-Pitaevskii simulation for $g=-0.9$. In the second and third columns, the color scale is adjusted for each snapshot to maintain contrast in the wave function, i.e., red always denotes the maximum remaining density and blue the minimum. The escape rate for each simulation is plotted at the bottom of each column. In the second and third columns, the color range (or grayscale range) is adjusted for each snapshot to maintain contrast in the wave function, i.e., in the color versions, red always denotes the maximum remaining density and blue the minimum. The escape rate for each simulation is plotted at the bottom of each column.

mean-field interaction energy between the atoms, where g measures the strength of the atom-atom interaction

$$g = 4\pi\hbar^2 a_0 N/Z. \tag{8}$$

Here, a_0 is the (scaled) atomic scattering length, N is the number of atoms in the condensate (since Ψ is normalized to unity), and Z is the thickness of the condensate in the z direction (assuming uniform density in the z direction). We consider an atomic species (such as ^{7}Li) that permits g to be adjusted from positive to negative through a Feschbach resonance.

We again choose the initial state to be a Gaussian of width σ_r, centered at $\mathbf{r}=0$ and with momentum expectation value $\mathbf{p}_{c0}$, i.e.,

$$\Psi_0(\mathbf{r}) = \frac{1}{\sqrt{2\pi}\sigma_r}\exp\left(\frac{i\mathbf{p}_{c0}\cdot\mathbf{r}}{\hbar}\right)\exp\left(-\frac{r^2}{4\sigma_r^2}\right). \tag{9}$$

The Wigner function $W_0(\mathbf{r},\mathbf{p})$ of this state agrees with the classical probability distribution (5).

We numerically propagate the wave packet forward in time using the standard fourth-order (symmetric) split-step algorithm. The grid size is typically taken to be $dx=dy=\hbar/4$ and the validity of the results was verified by using $dx=dy=\hbar/8$.

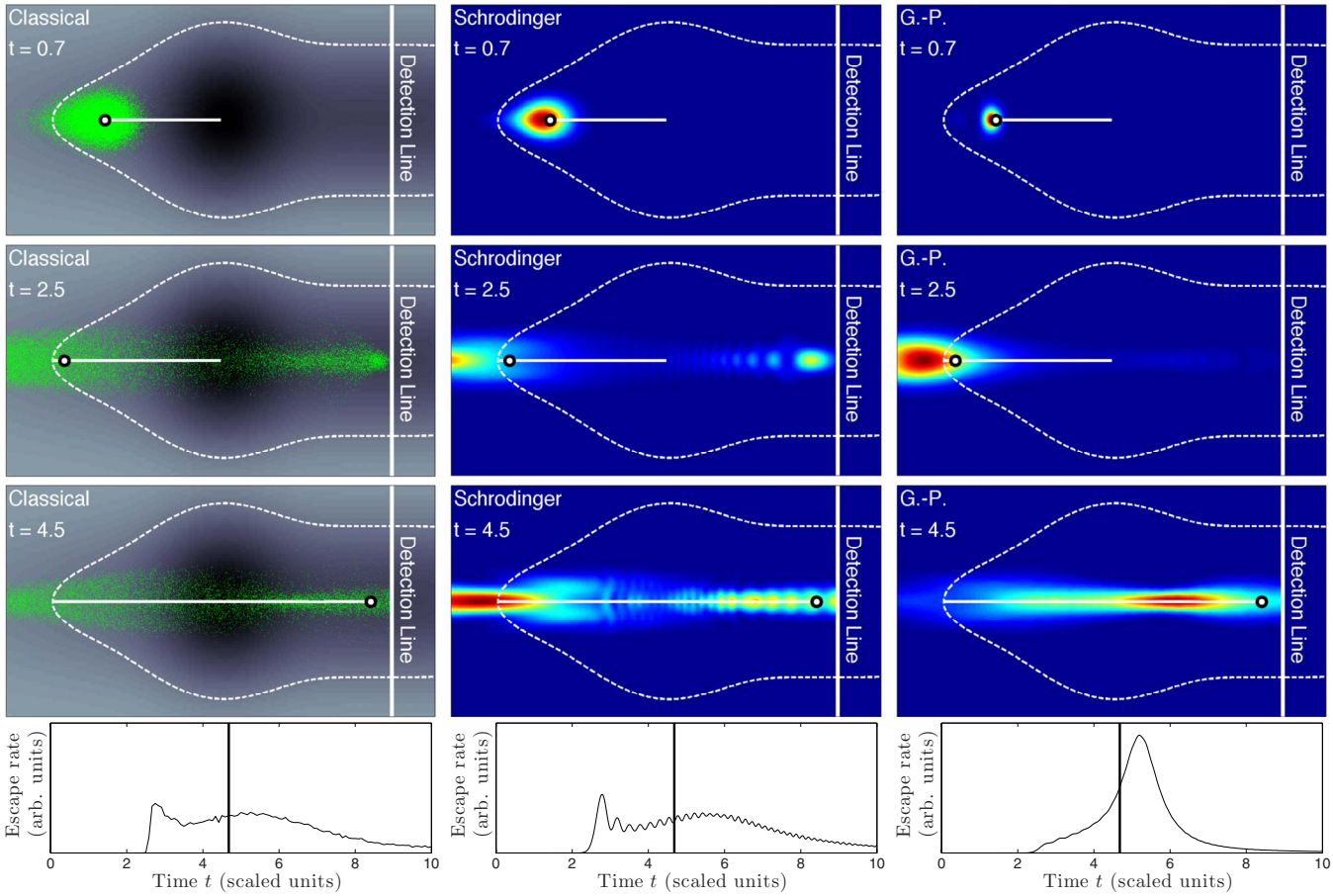

FIG. 4. (Color online) The evolution of the initial state as a function of time for launch angle $\theta=\pi$. Column 1 is a classical trajectory simulation using 5×10^4 trajectories; column 2 is the Schrödinger simulation; and column 3 is the Gross-Pitaevskii simulation for $g=-0.9g_{\mathrm{cr}}$.

The size of the actual computational domain $[x_{\min},x_{\max}]\times[y_{\min},y_{\max}]$ is quite larger than the domain $V(x,y)\leq E$ and well beyond the detection line $x=1$. In order to implement the escaping boundary conditions at $x=1$, we use a combination of (i) extending the profile of the potential at the detection line invariantly for $x>1$, and (ii) imposing a cutoff function for $x>1$, i.e., multiplying the solution by a parabolic function that decreases from 1 to 0 in $x\in[1,x_{\max}]$. A similar parabolic cutoff function is applied on the solution in the other three directions as well. By solving the same problem on a much larger computational domain, we verified that this method of implementing the boundary conditions does not introduce spurious numerical artifacts.

1. Schrödinger evolution

We first consider the case $g=0$, so that the (linear) Schrödinger equation applies. The second column of Fig. 3 shows the evolution of $|\Psi|^2$ for launch angle $\theta=0.85$. In the first frame, no considerable difference distinguishes the Schrödinger results from the adjacent classical result. In the second frame, the Schrödinger result still follows the classical density, but fringes are now evident, due to the interference of overlapping classical trajectories. Nevertheless, the plot of the Schrödinger escape rate differs little from the classical. This is because the interference fringes, being transverse to the detection line, average out upon integration. In the next two frames, the quantum density continues to follow the classical, but with interference fringes superposed.

2. Focusing Gross-Pitaevskii evolution

We now consider the influence of atom-atom interactions by using a nonvanishing g in the Gross-Pitaevskii equation. A positive g corresponds to a repulsive interaction, which would increase the dispersion of the state. We instead consider a negative g, which corresponds to an attractive interaction, thereby, forming a *focusing* nonlinearity, which reduces the dispersion of the packet. Since we have set $\int|\Psi|^2=1$, the necessary condition for collapse of the Gross-Pitaevskii Eq. (7) is $g<-g_{\mathrm{cr}}=-c\hbar^2$, where $c\approx5.85$ is derived from the two-dimensional Townes soliton [74]. Therefore, we choose $g=-0.9g_{\mathrm{cr}}$, which ensures that we are subcritical for collapse.

Using the same initial state given by Eq. (9), the third column of Fig. 3 shows the Gross-Pitaevskii evolution for $\theta=0.85$. In the first frame, the packet is significantly tighter than in the adjacent Schrödinger analysis. This continues to be evident in the second frame as well. In particular, the wave-packet spreading is reduced to such a degree that the

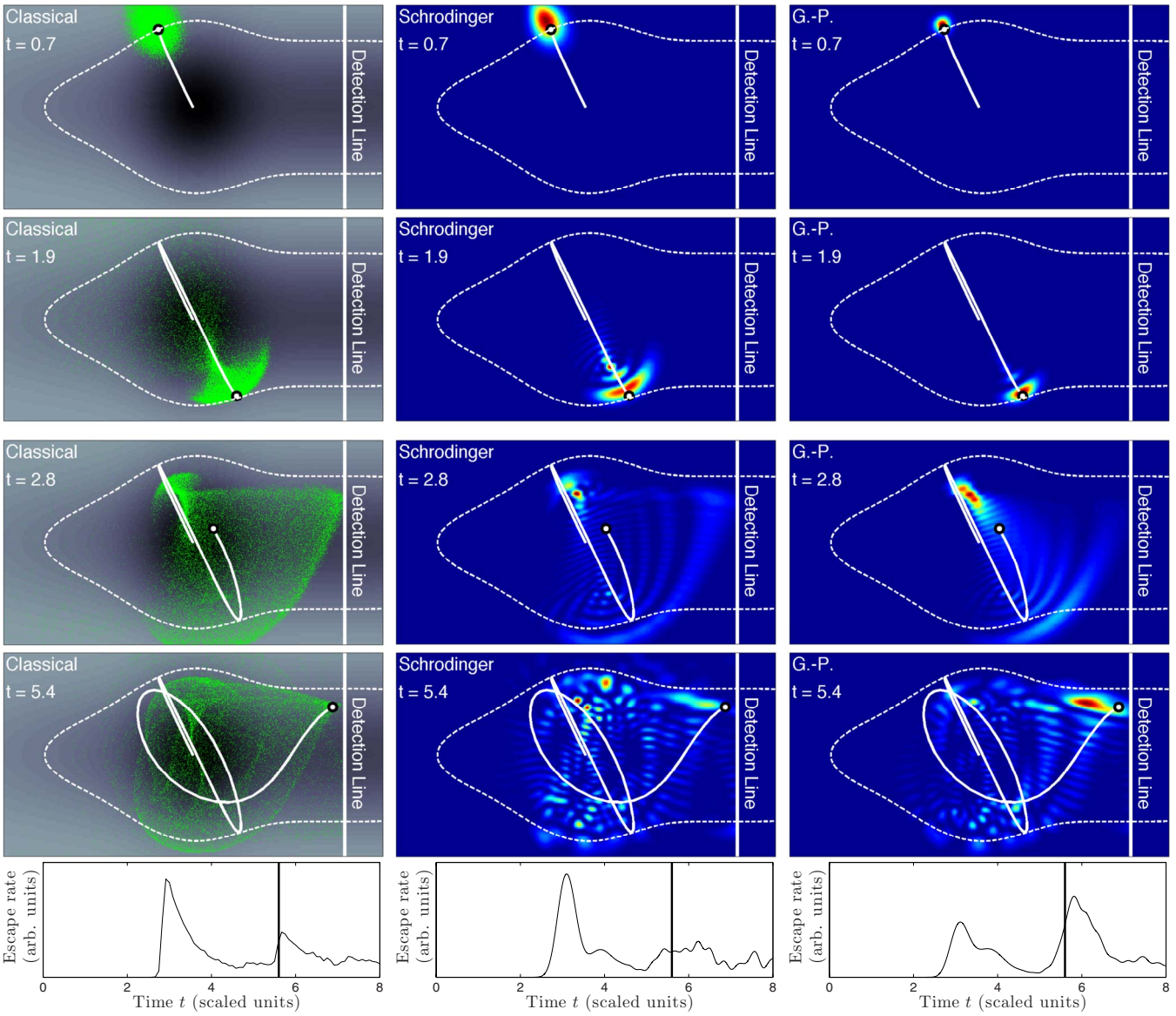

FIG. 5. (Color online) The evolution of the initial state as a function of time for launch angle $\theta=2.04$. Column 1 is a classical trajectory simulation using 5×10^4 trajectories; column 2 is the Schrödinger simulation; and column 3 is the Gross-Pitaevskii simulation for $g=-0.9g_{\mathrm{cr}}$.

interference fringes are essentially absent. Furthermore, though the escape-rate plot is similar to the previous two analyses, there is a slight shift in the escaping flux forward in time. We conclude, therefore, that the focusing nonlinearity causes the wave packet to track the central trajectory more faithfully. In subsequent frames, the wave packet eventually disperses and the Gross-Pitaevskii analysis more closely resembles the Schrödinger case.

C. Variation in escape dynamics with launch angle

The escape-time behavior changes dramatically as we adjust the launch angle of the initial state. For example, Fig. 4 shows the evolution for $\theta=\pi$. Focusing first on the classical ensemble in the first column, the central trajectory escapes around $t=4.5$, as seen by the vertical bar in the escape-rate plot. The central trajectory is associated with a broad pulse, whose maximum occurs just after the vertical bar. However, there is also a taller and sharper initial precursor pulse, which precedes the central trajectory. The precursor pulse is clearly visible near the detection line in the second frame. It has evidently reflected off the left side of the well before the broad pulse following the central trajectory.

Considering now the Schrödinger evolution in the second column, the quantum density again closely follows the classical density, but with interference fringes clearly overlaid in the second and third frames, once the wave packet has spread out horizontally. Since the interference fringes are now roughly parallel to the detection line, they are now recorded as oscillations in the escape-rate plot.

Turning now to the focusing Gross-Pitaevskii evolution in the third column, the packet has clearly spread less relative to the Schrödinger evolution. In particular, in the second frame there is essentially no precursor pulse near the detec-

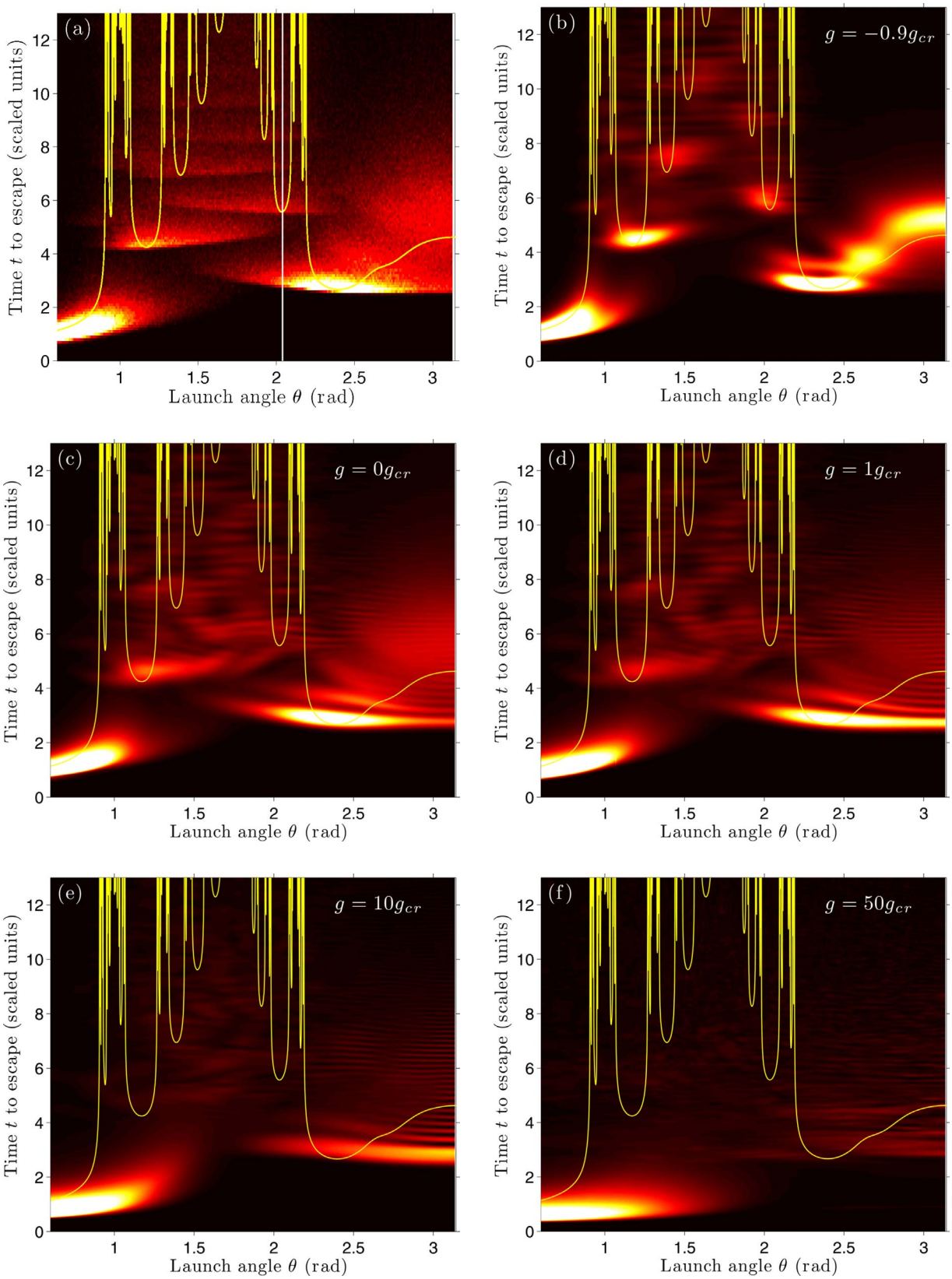

FIG. 6. (Color online) (a) The escape-time plot for an initial state modeled by a classical ensemble. 1×10^5 trajectories are used for each θ. (b) The escape-time plot for an initial quantum state modeled by the Gross-Pitaevskii equation with $g = -0.9g_{\mathrm{cr}}$. (c) The escape-time plot for an initial quantum state modeled by the Schrödinger equation ($g = 0$). Similarly, (d), (e), and (f) use $g/g_{\mathrm{cr}} = 1$, 10, and 50, respectively. In each plot, the shading records the escape rate in scaled variables. In order to increase the visibility of smaller flux values, the color scale is saturated so that the brightest white is used for all fluxes greater than 0.5.

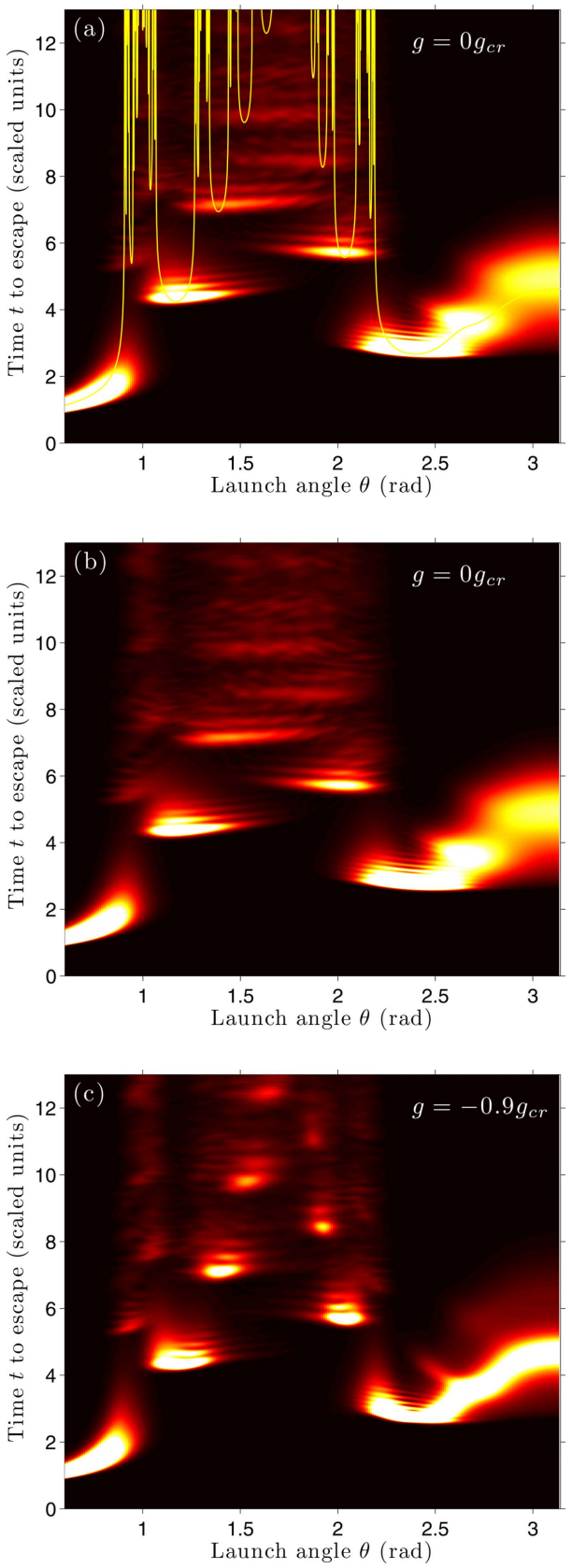

FIG. 7. (Color online) The escape-time plots computed for $\hbar = 0.004\,08$ and $g/g_{cr} = 0, -0.9$. (b) is identical to (a), except that the icicles are omitted to better visualize the clouds associated with the narrower icicles.

tion line. The missing precursor pulse is also clearly seen in the escape-rate plot, which now consists of a single sharpened pulse, escaping with the central trajectory. Thus, here the focusing nonlinearity eliminates the separation of the state into two pulses and causes the state to track the central trajectory more faithfully.

The third (and final) launch angle we shall consider explicitly is $\theta = 2.04$ (Fig. 5). The central trajectory undergoes a more complicated motion than the preceding two examples, exiting around $t = 5.4$. The classical escape-rate plot in the first column shows a pulse aligned with the vertical bar and, hence, associated with the central trajectory. However, by far the largest pulse is the much earlier initial pulse. In this case, the central trajectory does a rather poor job of predicting the escape-rate profile.

Considering now the Schrödinger evolution in the second column, the quantum density again clearly tracks the classical density, with interference fringes visible once the wave packet spreads out. Looking at the Schrödinger escape-rate plot, it roughly follows the classical plot, though quantum effects have reduced the clear peak aligned with the central trajectory.

Considering now the Gross-Pitaevskii evolution in the third column, we again see the expected narrowing of the pulse. In particular, in the Gross-Pitaevskii escape-rate plot, considerable flux has been shifted (compared to the Schrödinger plot) from the initial pulse to the (now prominent) pulse aligned with the central trajectory. Though we do not see focusing to a single pulse, as in Fig. 4, we do see that the focusing nonlinearity causes the state to more faithfully track the central trajectory.

The primary objective of this paper is to investigate the behavior of the escape-rate plots as θ is varied over a succession of angles. We thus run the preceding simulations over a large sampling of launch angles between 0 and π and then aggregate each of these escape-rate plots into a single escape-time plot in Fig. 6. First, we consider the escape rate for a classical ensemble shown in Fig. 6(a). The sharp thin curve plots the time for the central trajectory to escape, as in Fig. 2. The shading records the escape rate at time t for an initial state launched at angle θ. Thus, for a specific launch angle, say $\theta = 2.04$ marked by the vertical line, we can read off the escape rate as a function of time by simply moving up the vertical line and noting the intensity of the shading, which recovers the classical escape-rate plot in Fig. 5.

Notice that the shading (i.e., the escaping flux) closely follows the bottoms of each of the icicles. That is, the bottom of each icicle is blurred into a cloud, which covers a wider angular interval than the associated icicles. This blurring is a reflection of the fact that, due to the extended nature of an initial state launched at a given angle, such a state will be influenced by its neighboring icicles. This association between icicles and the blurred clouds is particularly evident for the wide icicles in the central zone of the plot. The shading obviously cannot resolve the detailed structure of the narrowest icicles. Nevertheless, the shading clearly records the basic self-similar structure of the main sequence of icicles.

Looking again at the two prominent pulses appearing in the classical escape-rate plot at the bottom of the first column

in Fig. 5, the large initial pulse can now be interpreted as arising from the cloud associated with the rightmost icicle in Fig. 6(a). The large size of the initial pulse is now seen to be due to the large width of the rightmost icicle. The second pulse, aligned with the central trajectory, is due to the icicle whose bottom is at about $t=5.5$. Since this icicle is much narrower, its cloud is less prominent and the corresponding pulse is smaller.

We next compare the classical escape-time plot to the Schrödinger ($g=0$) plot in Fig. 6(c). The bottoms of the widest icicles are again clearly blurred into clouds, following the basic classical structure. However, these clouds now have interference fringes superposed. Though the fringes complicate the correlation between icicles and shading, especially at later times, the connection can still be made for the four or five widest icicles.

We next compare the focusing ($g=-0.9g_{\mathrm{cr}}$) Gross-Pitaevskii escape-time plot in Fig. 6(b) to the Schrödinger plot. The Gross-Pitaevskii plot shows a remarkable shrinking of the clouds, greatly enhancing the correlation between the shading and the icicles. (The interference fringes are correspondingly also suppressed.) This correlation is also clearer than in the classical data Fig. 6(a). Thus, we come to our main conclusion. The focusing nonlinearity, due to its reduction in dispersion, significantly enhances the ability of quantum wave packets to resolve the underlying classical fractal structure in the escape dynamics.

For comparison, we also present the escape-time plots for several defocusing nonlinearities ($g/g_{\mathrm{cr}}=1,10,50$) in Figs. 6(d)–6(f). There is little difference between the $g=0$ and $g=g_{\mathrm{cr}}$ data, showing that moderate defocusing does not destroy the resolution. However, at $g=10g_{\mathrm{cr}}$, and certainly at $g=50g_{\mathrm{cr}}$, only the two largest icicles on the left and right are readily resolved.

V. DECREASING THE EFFECTIVE PLANCK'S CONSTANT

As mentioned in Sec. II, we can adjust the effective size of Planck's constant, while keeping the underlying (scaled) classical dynamics fixed, by adjusting the laser intensity and/or the physical size of the trap. By decreasing the effective Planck's constant, we become sensitive to finer-scale structure in the classical phase space, which provides another strategy, mentioned in Ref. [42], to increase the resolution of the fractal structure. Figures 7(a) and 7(b) show the escape-time plot for $g=-0.9g_{\mathrm{cr}}$ and for $\hbar=0.004\,08$, a factor of 5 smaller than in Fig. 6(c). We show the escape data both with and without the icicles superposed, so that the smaller clouds are not obscured by the icicles. The correlation between the icicles and clouds has clearly improved significantly by this modest reduction in $\hbar$. As $\hbar$ is decreased further, we would resolve more and more of the fine-scale structure, ultimately limited by experimental concerns. Reference [42] argued that $\hbar$ on the order of 10^{-5} should be physically achievable (with ^{87}Rb).

Finally, Fig. 7(c) includes the focusing nonlinearity for the smaller $\hbar$, showing a marked enhancement of the icicle resolution, both compared to Figs. 6(b) and 7(b).

VI. CONCLUSIONS

Building on Ref. [42], we considered the escape of a Bose-Einstein-condensed atomic ensemble from a chaotic double-Gaussian trap, as a function of the direction of the average momentum. The key advance here is to compute the impact of interference and atom-atom interactions on the resolution of the underlying classical fractal. Though interference complicates the fractal resolution somewhat, it is still clearly visible, especially for smaller $\hbar$. Attractive atom-atom interactions, however, can significantly enhance the fractal resolution.

Thus, we find two strategies for enhancing the fractal resolution. The first, discussed in Ref. [42], is simply to reduce the size of the state in phase space by decreasing the effective value of $\hbar$. This may be achieved either by increasing the size or the depth of the trap. The second, highlighted here, is to reduce the dispersion of the packet by increasing an attractive atom-atom interaction. This second strategy is limited by the fact that the interaction must remain subcritical to wave-packet collapse.

ACKNOWLEDGMENTS

The authors would like to thank Dan Steck and Lincoln Carr for their insights stimulating this analysis. This work was supported in part by NSF Grant No. PHY-0748828.

[1] W. R. S. Garton and F. S. Tomkins, Astrophys. J. **158**, 839 (1969).
[2] A. Holle, G. Wiebusch, J. Main, B. Hager, H. Rottke, and K. H. Welge, Phys. Rev. Lett. **56**, 2594 (1986).
[3] J. Main, G. Wiebusch, A. Holle, and K. H. Welge, Phys. Rev. Lett. **57**, 2789 (1986).
[4] A. Holle, J. Main, G. Wiebusch, H. Rottke, and K. H. Welge, Phys. Rev. Lett. **61**, 161 (1988).
[5] M. L. Du and J. B. Delos, Phys. Rev. A **38**, 1896 (1988).
[6] M. L. Du and J. B. Delos, Phys. Rev. A **38**, 1913 (1988).
[7] J. Main, G. Wiebusch, K. Welge, J. Shaw, and J. B. Delos, Phys. Rev. A **49**, 847 (1994).
[8] D. Kleppner and J. B. Delos, Found. Phys. **31**, 593 (2001).
[9] J. E. Bayfield and P. M. Koch, Phys. Rev. Lett. **33**, 258 (1974).
[10] J. E. Bayfield, L. D. Gardner, and P. M. Koch, Phys. Rev. Lett. **39**, 76 (1977).
[11] R. V. Jensen, S. M. Susskind, and M. M. Sanders, Phys. Rep. **201**, 1 (1991).
[12] P. M. Koch and K. A. H. van Leeuwen, Phys. Rep. **255**, 289 (1995).
[13] F. B. Dunning, J. C. Lancaster, C. O. Reinhold, S. Yoshida, and J. Burgdörfer, Adv. At., Mol., Opt. Phys. **52**, 49 (2005).

[14] S. Yoshida, C. O. Reinhold, E. Persson, J. Burgdörfer, and F. B. Dunning, J. Phys. B **38**, S209 (2005).
[15] W. Zhao, J. J. Mestayer, J. C. Lancaster, F. B. Dunning, C. O. Reinhold, S. Yoshida, and J. Burgdörfer, Phys. Rev. Lett. **95**, 163007 (2005).
[16] K. A. Mitchell, J. P. Handley, B. Tighe, A. Flower, and J. B. Delos, Phys. Rev. Lett. **92**, 073001 (2004).
[17] K. A. Mitchell, J. P. Handley, B. Tighe, A. Flower, and J. B. Delos, Phys. Rev. A **70**, 043407 (2004).
[18] T. Topcu and F. Robicheaux, J. Phys. B **40**, 1925 (2007).
[19] K. Burke and K. A. Mitchell, Phys. Rev. A **80**, 033416 (2009).
[20] J. U. Nöckel and A. D. Stone, Nature (London) **385**, 45 (1997).
[21] C. Gmachl, F. Capasso, E. E. Narimanov, J. U. Nöckel, A. D. Stone, J. Faist, D. L. Sivco, and A. Y. Cho, Science **280**, 1556 (1998).
[22] P. L. Boyland, H. Aref, and M. A. Stremler, J. Fluid Mech. **403**, 277 (2000).
[23] J.-L. Thiffeault, Phys. Rev. Lett. **94**, 084502 (2005).
[24] J.-L. Thiffeault and M. D. Finn, Philos. Trans. R. Soc. London, Ser. A **364**, 3251 (2006).
[25] S. Balasuriya, Phys. Fluids **17**, 118103 (2005).
[26] See the special journal issue, including the overview by S. Wiggins and J. M. Ottino, Philos. Trans. R. Soc. London, Ser. A **362**, 937 (2004).
[27] W. S. Koon, M. W. Lo, J. E. Marsden, and S. D. Ross, Chaos **10**, 427 (2000).
[28] C. Jaffé, S. D. Ross, M. W. Lo, J. Marsden, D. Farrelly, and T. Uzer, Phys. Rev. Lett. **89**, 011101 (2002).
[29] R. Blümel and W. P. Reinhardt, *Chaos in Atomic Physics* (Cambridge University Press, Cambridge, UK, 1997).
[30] M. G. Raizen, Adv. At., Mol., Opt. Phys. **41**, 43 (1999).
[31] A. Buchleitner, M. B. d'Arcy, S. Fishman, S. A. Gardiner, I. Guarneri, Z.-Y. Ma, L. Rebuzzini, and G. S. Summy, Phys. Rev. Lett. **96**, 164101 (2006).
[32] M. B. d'Arcy, G. S. Summy, S. Fishman, and I. Guarneri, Phys. Scr. **69**, C25 (2004).
[33] M. B. d'Arcy, R. M. Godun, M. K. Oberthaler, D. Cassettari, and G. S. Summy, Phys. Rev. Lett. **87**, 074102 (2001).
[34] D. A. Steck, W. H. Oskay, and M. G. Raizen, Science **293**, 274 (2001).
[35] D. A. Steck, W. H. Oskay, and M. G. Raizen, Phys. Rev. Lett. **88**, 120406 (2002).
[36] H. Ammann, R. Gray, I. Shvarchuck, and N. Christensen, Phys. Rev. Lett. **80**, 4111 (1998).
[37] G. H. Ball, K. M. D. Vant, H. Ammann, and N. L. Christensen, J. Opt. B: Quantum Semiclassical Opt. **1**, 357 (1999).
[38] K. Vant, G. Ball, H. Ammann, and N. Christensen, Phys. Rev. E **59**, 2846 (1999).
[39] M. E. K. Williams, M. P. Sadgrove, A. J. Daley, R. N. C. Gray, S. M. Tan, A. S. Parkins, N. Christensen, and R. Leonhardt, J. Opt. B: Quantum Semiclassical Opt. **6**, 28 (2004).
[40] V. Milner, J. L. Hanssen, W. C. Campbell, and M. G. Raizen, Phys. Rev. Lett. **86**, 1514 (2001).
[41] N. Friedman, A. Kaplan, D. Carasso, and N. Davidson, Phys. Rev. Lett. **86**, 1518 (2001).
[42] K. A. Mitchell and D. A. Steck, Phys. Rev. A **76**, 031403(R) (2007).
[43] L. Khaykovich, F. Schreck, G. Ferrari, T. Bourdel, J. Cubizolles, L. D. Carr, Y. Castin, and C. Salomon, Science **296**, 1290 (2002).
[44] K. E. Strecker, G. B. Partridge, A. G. Truscott, and R. G. Hulet, Nature (London) **417**, 150 (2002).
[45] L. D. Carr and J. Brand, Phys. Rev. Lett. **92**, 040401 (2004).
[46] P. Gaspard, *Chaos, Scattering and Statistical Mechanics* (Cambridge University Press, Cambridge, 1998).
[47] L. Gottdiener, Mol. Phys. **29**, 1585 (1975).
[48] D. W. Noid, S. K. Gray, and S. A. Rice, J. Chem. Phys. **84**, 2649 (1986).
[49] J.-M. Petit and M. Henon, Icarus **66**, 536 (1986).
[50] B. Eckhardt and C. Jung, J. Phys. A **19**, L829 (1986).
[51] B. Eckhardt, J. Phys. A **20**, 5971 (1987).
[52] C. Jung and H. J. Scholz, J. Phys. A **20**, 3607 (1987).
[53] P. Gaspard and S. Rice, J. Chem. Phys. **90**, 2225 (1989).
[54] B. Ruckerl and C. Jung, J. Phys. A **27**, 55 (1994).
[55] B. Ruckerl and C. Jung, J. Phys. A **27**, 6741 (1994).
[56] C. Lipp and C. Jung, J. Phys. A **28**, 6887 (1995).
[57] C. Jung, C. Lipp, and T. H. Seligman, Ann. Phys. **275**, 151 (1999).
[58] A. Tiyapan and C. Jaffé, J. Chem. Phys. **99**, 2765 (1993).
[59] A. Tiyapan and C. Jaffé, J. Chem. Phys. **101**, 10393 (1994).
[60] A. Tiyapan and C. Jaffé, J. Chem. Phys. **103**, 5499 (1995).
[61] K. A. Mitchell, J. P. Handley, B. Tighe, S. K. Knudson, and J. B. Delos, Chaos **13**, 880 (2003).
[62] K. A. Mitchell, J. P. Handley, S. K. Knudson, and J. B. Delos, Chaos **13**, 892 (2003).
[63] K. A. Mitchell and J. B. Delos, Physica D **221**, 170 (2006).
[64] K. A. Mitchell, Physica D **238**, 737 (2009).
[65] P. Collins, in *Geometry and Topology in Dynamics*, Contemporary Mathematics Vol. 246 (American Mathematical Society, Providence, RI, 1999), pp. 65–86.
[66] P. Collins, Int. J. Bifurcation Chaos Appl. Sci. Eng. **12**, 605 (2002).
[67] P. Collins, Dyn. Syst. **19**, 1 (2004).
[68] P. Collins, Exp. Math. **14**, 75 (2005).
[69] E. J. Heller, J. Chem. Phys. **94**, 2723 (1991).
[70] R. G. Littlejohn, Phys. Rep. **138**, 193 (1986).
[71] S. Habib, e-print arXiv:quant-ph/0406011.
[72] C. J. Pethick and H. Smith, *Bose-Einstein Condensation in Dilute Gases* (Cambridge University Press, Cambridge, 2002).
[73] L. Pitaevskii and S. Stringari, *Bose-Einstein Condensation* (Oxford University Press, Oxford, 2003).
[74] C. Sulem and P.-L. Sulem, *Nonlinear Schrödinger Equations: Self-Focusing and Wave Collapse* (Springer, New York, 1999).